Error analysis and comparison of Riemann and average fluxes for a spacetime discontinuous Galerkin electromagnetic formulation

Reza Abedi*[(1)], Saba Mudaliar[(2)]

(1) University of Tennessee Space Institute (UTSI), Tullahoma, TN, 37355, www.rezaabedi.info, rabedi@utsi.edu
(2) Sensors Directorate, Air Force Research Laboratory, Wright-Patterson AFB, Dayton, OH 45433, saba.mudaliar@us.af.mil

Abstract

We present a time domain discontinuous Galerkin (TDDG) method for electromagnetics problem that directly discretizes space and time by unstructured grids satisfying a specific causality constraint. This enables a local and asynchronous solution procedure. We show that the numerical method is dissipative, thus ensuring its stability. Numerical results show the convergence rate of 2p + 1 for energy dissipation. We also investigate the choice of Riemann versus average numerical fluxes for noncausal faces and demonstrate that while the more dissipative nature of Riemann fluxes may render it unsuitable for low order elements, it provides a cleaner solution for high order elements.
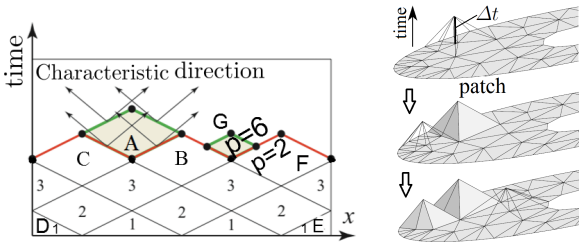
1 Spacetime discontinuous Galerkin method

Figure 1. Spacetime discretization used in the SDG method.

Figure 2. Patch-by-patch solution procedure.

We present a *spacetime discontinuous Galerkin* (SDG) method that directly discretizes the spacetime using unstructured grids. Many exceptional properties of the method stem from the use of *causal* meshes. For example, in the fig. 1 the solution of element A depends only on the solution of earlier elements B and C given that the red facets are causal (fastest waves shown in arrows only pass in one direction through the facet). The level-1 elements depend only on initial conditions and boundary conditions for the elements D and E. The level-1 element solutions can be computed locally and in parallel. Thus, causal SDG meshes enable asynchronous, element-by-element solutions with linear solution complexity.

We replace the individual elements in the $1d \times$time with small clusters of simplicial elements called *patches*, where only the exterior patch facets need to be causal as shown in

fig. 2 for clusters of tetrahedral elements in $2d \times$time. Using an advancing-front procedure, in each step the *TentPitcher* algorithm [1, 2] advances in time a vertex in the *front mesh* to define a local front update; the causality constraint limits the maximum time increment Δt at the vertex. We solve new patches as local problems and update the current front, until the entire spacetime analysis domain is solved.

2 EM formulation

While the formulation of the SDG method is outside the scope of this manuscript, we briefly discuss the key components of our formulation. The finite elements are discretized with discontinuous basis functions that form complete polynomials of order p in spacetime. The electric field **E** and magnetic field **H** are discretized and electric and magnetic flux densities **D** and **B** are obtained from constitutive equations. For example, for an isotropic material $\mathbf{D} = \varepsilon\mathbf{E}$ and $\mathbf{B} = \mu\mathbf{H}$. As customary, only Ampère and Faraday laws from Maxwell's equation are discretized from the Maxwell's equation. Since the basis functions are discontinuous across element boundaries, both the partial differential equations and their corresponding jump conditions are discretized and weakly enforced in an element $\mathcal{Q}$ and its boundary $\partial\mathcal{Q}$. After the application of Stokes theorem, the discrete weak form is obtained,

$$
\begin{aligned}
&\int_{\partial\mathcal{Q}} \left\{ \left(\hat{\mathbf{E}}.\mathbf{D}^* + \hat{\mathbf{H}}.\mathbf{B}^*\right) \star \mathrm{d}t + \left(\hat{\mathbf{E}} \times \mathbf{H}^* - \hat{\mathbf{H}} \times \mathbf{E}^*\right) \star \mathbf{dx} \right\} \\
&+ \int_{\mathcal{Q}} \left\{ \left(-\dot{\hat{\mathbf{E}}}.\mathbf{D}^h - \nabla \times \hat{\mathbf{E}}.\mathbf{H}^h + \hat{\mathbf{E}}.\mathbf{J}^h\right) \right. \\
&\left. + \left(-\dot{\hat{\mathbf{H}}}.\mathbf{B}^h + \nabla \times \hat{\mathbf{H}}.\mathbf{E}^h\right) \right\} \boldsymbol{\Omega} = \mathbf{0}
\end{aligned}
\tag{1}
$$

where **J** is the electric current density. The $\hat{\ }$ and $.^h$ correspond to weight and discrete solution fields, respectively. The $.^*$ fields are target fields on element boundaries that are obtained from the solution to a local Riemann problem. The 3-form $\boldsymbol{\Omega}$ resembles the volume differential in $\mathcal{Q}$ and and 2-forms $\star\mathbf{dx}$ and $\star\mathrm{d}t$ can be related to spatial and temporal components of normal vector times surface differential on $\partial\mathcal{Q}$ if spacetime normal vectors could be defined.

3 Numerical fluxes

For a noncausal d-manifold Γ in $\mathcal{D}$, the characteristics pass through the interface from the opposite side. In discrete
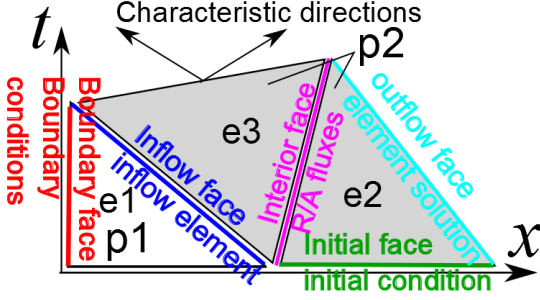
Figure 3. Different face types for spacetime elements. Patches p1 and p2 include one and two elements.

setting, the interior facets of a patch can be noncausal. An example is the interior faces of two elements in patch p2 in fig. 3. For these faces the target solution depends on traces from the two sides $\mathbf{U}^{\pm} = (\mathbf{E}^{\pm}, \mathbf{H}^{\pm})$ and the orientation of Γ. Herein, we only consider solutions for isotropic materials with electrical permittivities $\varepsilon^{\pm}$ and magnetic permeabilities $\mu^{\pm}$. Impedance Z, admittance Y, and wave speeds c are $Z^{\pm} = 1/Y^{\pm} = \sqrt{(\mu/\varepsilon)^{\pm}}$ and $c^{\pm} = 1/\sqrt{(\mu\varepsilon)^{\pm}}$. We consider two choices of Riemann and average fluxes for target values. Riemann fluxes are obtained by solving a 1D electromagnetic problem with initial conditions consistent with the traces of the solution from the two sides of the interface. The solutions for tangential components of $\mathbf{E}$ and $\mathbf{H}$ on a noncausal interface, *e.g.,* interior face of the patch p2 in fig. 3, are

$$\mathbf{n} \times \mathbf{E}^R = \mathbf{n} \times \frac{(Y\mathbf{E} - \mathbf{n} \times \mathbf{H})^- + (Y\mathbf{E} + \mathbf{n} \times \mathbf{H})^+}{Y^- + Y^+} \quad (2a)$$

$$\mathbf{n} \times \mathbf{H}^R = \mathbf{n} \times \frac{(Z\mathbf{H} + \mathbf{n} \times \mathbf{E})^- + (Z\mathbf{H} - \mathbf{n} \times \mathbf{E})^+}{Z^- + Z^+} \quad (2b)$$

where $\mathbf{n}$ is the spatial normal vector to an interface. In contrast, the average fluxes are the averages of the two sides,

$$\mathbf{n} \times \mathbf{E}^R = \mathbf{n} \times \frac{\mathbf{E}^- + \mathbf{E}^+}{2}, \quad \mathbf{n} \times \mathbf{H}^R = \mathbf{n} \times \frac{\mathbf{H}^- + \mathbf{H}^+}{2} \quad (3)$$

For both flux options, the normal components E^1 and H^1 are obtained by enforcing the continuity of D_1 and B_1 across the interface, based on Gauss divergence laws for electric and magnetic field densities. For conventional DG methods these fluxes are inactive as the noncausal interfaces are conceptually vertical. However, for arbitrary nonvertical noncausal facets in our spacetime grids, the side with earlier solution specifies D_1 and B_1 which in turn provides the target solutions for E^1 and H^1. For example in fig. 3 and for the interior interface of patch p2, the element e2 provides target solutions for D_1 and B_1.

4 Error norms

The spacetime electromagnetic energy flux $\boldsymbol{N} := \boldsymbol{u} + \boldsymbol{S}$ combines *electromagnetic energy density form* $\boldsymbol{u} = \frac{1}{2}(\mathbf{E}.\mathbf{D} + \mathbf{H}.\mathbf{B})\star dt$ and Poynting form $\boldsymbol{S} := \boldsymbol{E} \wedge \boldsymbol{H} = \mathbf{E} \times \mathbf{H}\star\mathbf{dx}$. The energy dissipation for an arbitrary spacetime volume $\mathscr{Q}$ is,

$$\Delta_{\mathscr{Q}} := -\left[\int_{\partial \mathscr{Q}} \boldsymbol{N}(\boldsymbol{U}^*) + \int_{\mathscr{Q}} \boldsymbol{R}_N\right] \quad (4)$$

where $\boldsymbol{U}^*$ is the physically correct flux on $\partial \mathscr{Q}$ the boundary of $\mathscr{Q}$ and $\boldsymbol{R}_N := \mathbf{E}.\mathbf{J}\boldsymbol{\Omega}$ is the *energy balance source term*. In discrete setting $\boldsymbol{N}$ is expressed in terms of target fluxes for $\boldsymbol{U}^*$ which are obtained from (2) or (3) and energy dissipation in fact can be nonzero. Through a relatively long derivation that uses certain symmetries of constitutive parameters for a bi-anisotropic material one can show,

$$\Delta_{\mathscr{Q}} = -\int_{\partial \mathscr{Q}} \frac{1}{2}\left([\![\mathbf{E}]\!][\![\mathbf{D}]\!][\![\mathbf{H}]\!][\![\mathbf{B}]\!]\right)\star dt + [\![\mathbf{E}]\!] \times [\![\mathbf{H}]\!]\star\mathbf{dx} \quad (5)$$

where $[\![\mathbf{E}]\!] = \mathbf{E}^* - \mathbf{E}^h$ is the jump between the target flux on the boundary of a spacetime element $\mathscr{Q}$ and the trace of interior discrete solution $\mathbf{E}^h$ and same applies to other fields $\mathbf{H}, \mathbf{D}, \mathbf{B}$. To prove non-negativity of (5) we consider all different cases of element facets, as shown in fig. 3. On causal outflow facets target solutions are equal to element solutions, $.^* = .^h$ so the contribution of outflow facets to the right hand side (RHS) of (5) is zero. The faces on the boundary of the domain are vertical and only $[\![\mathbf{E}]\!] \times [\![\mathbf{H}]\!]\star\mathbf{dx}$ is present. This term is zero as one of both $[\![\mathbf{E}]\!]$ and $[\![\mathbf{H}]\!]$ are zero for any given direction for all the common forms of boundary conditions. For the inflow facets, the target values are set to the earlier traces from neighbor inflow element or initial condition. The non-negativity of (5) is proven by using the causality, *i.e.,* shallow slope, of the inflow facet. For interior (noncausal) faces, there are two cases. First, if there is a material interface the face is vertical and similar to domain boundary faces only $[\![\mathbf{E}]\!] \times [\![\mathbf{H}]\!]\star\mathbf{dx}$ is present. By directly plugging Riemann solutions, one can observe that this term is non-negative so the energy dissipation on an interior face is. For nonvertical noncausal faces, the normal components E^1, H^1, D_1, B_1 are also present through the first term in (5). The proof of non-negativity of the integrand for these faces uses the facts that D_1 and B_1 are enforced with respect to earlier solution and that the two sides are the same material ($Z^- = Z^+$). Since the integral is nonnegative for all face types so is the dissipation for one element $\mathscr{Q}$. The *total energy dissipation* over $\mathscr{D}$, denoted by Δ, is given by $\Delta := -[\int_{\partial \mathscr{D}} \boldsymbol{N}(\boldsymbol{U}^*) + \int_{\mathscr{D}} \boldsymbol{R}_N] = \sum_{\mathscr{Q} \in \mathscr{P}_h} \Delta_{\mathscr{Q}} \geq 0$ Since $\Delta_{\mathscr{Q}} \geq 0$ so is Δ, hence the method is dissipative and energetically stable.

When average fluxes (3) are used, the dissipations on the two sides of an interior noncausal face are opposite of each other. With Riemann fluxes the energy dissipation is non-negative on each side whereas with Average fluxes the sum of dissipation for this face from the two sides is zero. This implies a more dissipative nature for the Riemann flux option. On the other hand, we no longer have non-negative dissipation per element with average fluxes. Instead the weaker non-negativity condition is satisfied per each patch $\mathscr{P}$ of elements, which again clearly guarantees the domains non-negative dissipation as Δ can also be expressed as $\Delta = \sum_{\mathscr{P}} \Delta_{\mathscr{P}} \geq 0$.

5 Convergence studies

For convergence studies of the method we use the analytical solution, $\mathbf{E} = \mathscr{E}\cos(\omega t - \mathbf{k}.\mathbf{x})$ $\mathbf{H} = \mathscr{H}\cos(\omega t - \mathbf{k}.\mathbf{x})$ with

a wavenumber vector $\mathbf{k}$ with $|\mathbf{k}| = 1$ and frequency $\omega = c|\mathbf{k}|$. The wave speed $c = 1/\sqrt{\varepsilon\mu} = 1$ for a domain with $\varepsilon = 1$, $\mu = 1$. The eigenvectors $\mathscr{E}, \mathscr{H}$, and $\mathbf{k}$ are mutually orthogonal and different values are chosen for different 1D to 3D electromagnetic formulations.

Figure 4 presents the convergence of SDG solutions with respect to energy dissipation Δ for $d = 1$ to 3. The horizontal axis of all the plots corresponds to h the element size for the uniform grids used. The elements are interpolated with complete polynomials in spacetime of order p. For example, in $\mathbb{E}^2 \times \mathbb{R}$ the solutions for $\mathbf{E}$ and $\mathbf{H}$ of a $p = 2$ cover the space spanned by $\{1, x_1, x_2, t, x_1^2, x_1 x_2, x_1 t, x_2^2, x_2 t, t^2\}$. While the convergence rates are slightly higher for $d = 2$ and slightly lower for $d = 3$, in general the results confirm the predicted convergence rate of $2p + 1$. In comparison a convergence rate of $2p - 1$ for energy dissipation was reported for elastodynamic problem in [3]. In the latter, terms appearing in energy dissipation were derivative of the primary field displacement, while in electromagnetics formulation $\mathbf{E}$ and $\mathbf{H}$ appearing in (5) are directly interpolated. This explains the higher convergence rate.
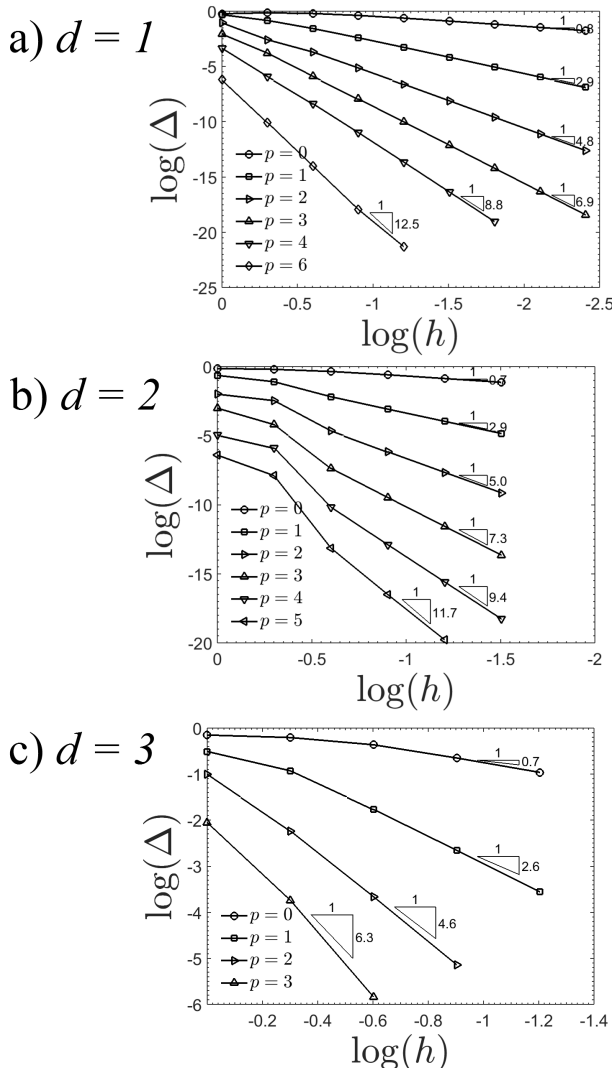

Figure 4. Energy dissipation convergence rates for the approximation of a smooth solution for $d = 1, 2, 3$.

5.1 The choice for target values

The main purpose of this section is to study the impact of the choice of target fluxes on discrete solution. Some results in the literature, *cf. e.g.,* [3], suggest that for problems with infinitely smooth solution there is not much difference in the solutions obtained from average and Riemann flux options. That is why we choose a problem with strong discontinuities in $\mathbf{E}$ and $\mathbf{H}$ fields induces by propagation of a step function and its transition/reflection at a bimaterial interface. This 1D problem involves a domain of unit length with two different materials with $\varepsilon_l = 1, \mu_l = 1$ and $\varepsilon_r = 10, \mu_r = 1$ on the left and right side of an interface at $x_I = 0.5$. The domain is loaded from the left side with a boundary condition $E^3 = 1$. We compare the convergence of solutions, by uniform h-refinement or p-enrichment, at target time $t_f = 0.8$.
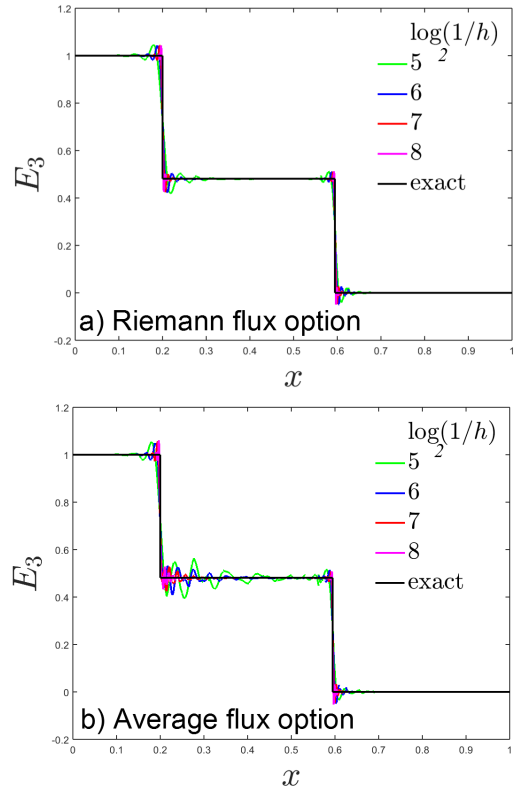

Figure 5. Convergence of E^3 with uniform h-refinement for the 1D problem with nonsmooth solution and $p = 4$.

Figure 5 shows how the results for both flux options tend to the exact solution through uniform h-refinement for element polynomial order $p = 4$. In fig. 5 we observe that the solutions with Riemann flux option are much better in the middle segment, especially for coarsest grids with $log_2(1/h) = 5, 6$. Obviously, in either case the solutions get more accurate as element size decreases.

Figure 6 depicts the convergence of the solution for E^3 for mesh size $h = \frac{1}{32}$ and various polynomial orders. Compared to fig. 6a), and similar to previous case, we observe that the results with average flux in fig. 6b) contain large zones of

high oscillation particularly in the middle segment. In either case, as expected the solutions tend to the exact solution by p-enrichment.
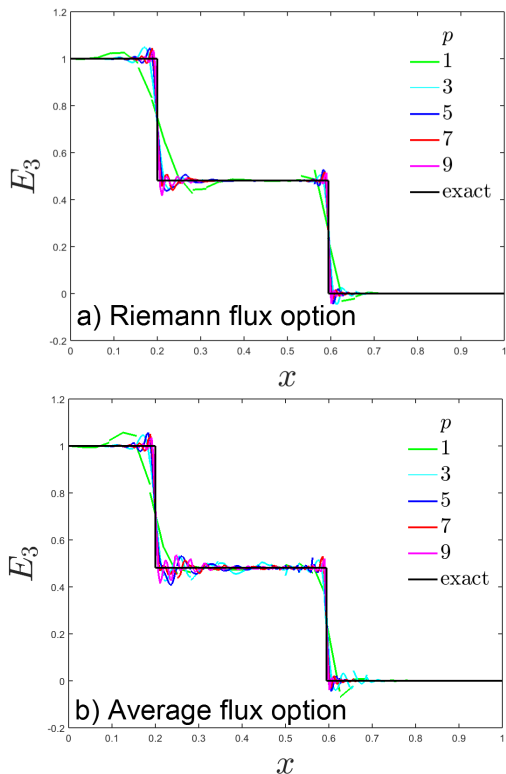

Figure 6. Convergence of E^3 with uniform p-enrichment for the 1D problem with nonsmooth solution and $h = \frac{1}{32}$.
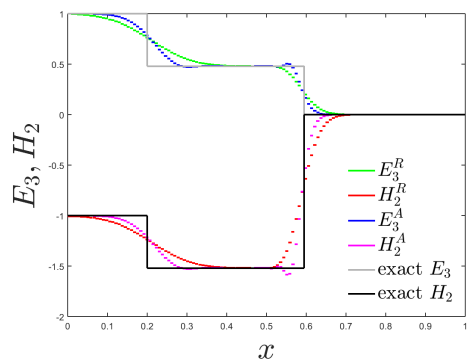

Figure 7. Comparison of solutions with different flux options and $p = 0, h = \frac{1}{128}$.

The fact that the solutions with Riemann fluxed are more damped and less oscillatory can be viewed in the next two figures. In fig. 7 results for $p = 0$ and $h = \frac{1}{128}$ are compared between Riemann and Average flux options. There is a slight overshoot and undershoot in E^3 and H^2 near $x = 0.2$ for Average flux option, however other than that, in this case the solutions from Average flux option are more accurate as the solutions with Riemann flux option are overly damped. Figure 8 compares the solutions now for the high polynomial order $p = 9$ at the mesh resolution $h = \frac{1}{32}$ around $x = 0.2$. In this case, we observe that for both E^3, H^2 the solutions obtained with Riemann flux option much more closely follow the exact solution line; in contrast, those ob-

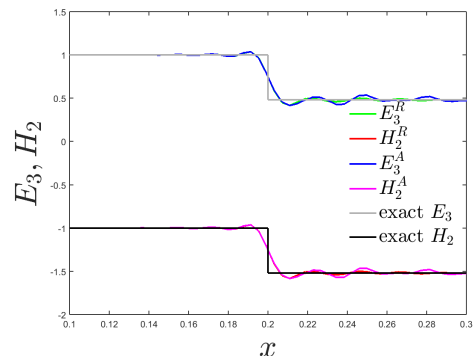tained with Average fluxes show a wider oscillations around the constant solution value for $x > 0.2$.

Figure 8. Comparison of solutions with different flux options and $p = 9, h = \frac{1}{32}$.

6   Conclusions

We have presented a spacetime discontinuous Galerkin method for linear electromagnetics. If elements can be arranged in small patches of elements whose exterior boundaries inside the spacetime domain are causal, the solution process is asynchronous and local with linear complexity in terms of number of elements. We provided a sketch of the method's stability by showing that discrete dissipation is equal to an integral on the facets of the elements that is a function of jump terms between target solutions and their corresponding interior traces of the solution. The integral can be shown to be nonnegative for different types of element facet, thus implying the method's energetic stability. We compared the choice of Riemann versus average fluxes on noncausal faces of elements by studying the solution of a problem with strong discontinuities in electromagnetic fields. It was demonstrated that the Riemann fluxes resulted in overly dissipated solutions for low polynomial orders, but at high orders they outperformed average flux option by yielding smoother solutions.

References

[1] R. Abedi, S.H. Chung, J. Erickson, Y. Fan, M. Garland, D. Guoy, R.B. Haber, J.M. Sullivan, S. Thite, and Y. Zhou. Spacetime meshing with adaptive refinement and coarsening. In *Proceedings of the Twentieth Annual Symposium on Computational Geometry*, SCG '04, pages 300–309. ACM, June 9-11 2004.

[2] R. Abedi, R. B. Haber, S. Thite, and J. Erickson. An h–adaptive spacetime–discontinuous Galerkin method for linearized elastodynamics. *Revue Européenne de Mécanique Numérique (European Journal of Computational Mechanics)*, 15(6):619–642, 2006.

[3] Reza Abedi, Robert B. Haber, and Boris Petracovici. A spacetime discontinuous Galerkin method for elastodynamics with element-level balance of linear momentum. *Computer Methods in Applied Mechanics and Engineering*, 195:3247–3273, 2006.